Nuclear Materials and Energy 25 (2020) 100790

Contents lists available at ScienceDirect

Nuclear Materials and Energy

journal homepage: www.elsevier.com/locate/nme

Sequential ion irradiations on Fe-Cr and ODS Fe-Cr alloys

M. Šćepanović[a,*], T. Leguey[a], I. García-Cortés[b], F.J. Sánchez[b], C. Hugenschmidt[c], M.A. Auger[a], V. de Castro[a]

[a] Departamento de Física. Universidad Carlos III de Madrid, 28911 Leganés, Spain
[b] Laboratorio Nacional de Fusión, CIEMAT, Avda. de la Complutense 40, 28040 Madrid, Spain
[c] FRM II and Physics Department, Technische Universität München, 85747 Garching, Germany

ARTICLE INFO

Keywords:
FeCr alloys
ODS steels
Ion irradiation
Radiation damage
Transmission electron microscopy
Positron annihilation spectroscopy

ABSTRACT

Oxide dispersion strengthened steels are candidate materials for nuclear reactor applications due to a powerful combination of properties, such as reduced activation, high-temperature strength and increased creep resistance. The dispersion of nanometric oxide particles in the steel matrix may also enhance radiation resistance by acting as trapping sites for irradiation induced defects. In this work, an Fe–14Cr–2 W–0.3-Ti–0.3Y_2O_3 (wt%) steel and a model Fe-14Cr (wt%) alloy were sequentially irradiated with He^+ and Fe^+ ions up to 15 dpa and 8000 appm to simulate fusion radiation damage. Their microstructural stability was investigated by positron annihilation spectroscopy and transmission electron microscopy. Transmission electron microscopy studies show that under these irradiation conditions there are no significant changes in the mean size, qualitative chemical composition and number density of nanoparticles, although the irradiation appears to induce a slight coarsening of the smaller nanoparticles. Both materials exhibit very small (< 2 nm) irradiation-induced bubbles, with similar sizes but lower number density in the ODS steel. Positron annihilation spectroscopy results show the presence of irradiation induced open volume defects, much more noticeable in the model alloy. In both alloys, helium appears to associate with the newly formed vacancy-type defects introduced by the subsequent Fe^+ irradiation.

1. Introduction

In-vessel structural materials for nuclear fusion power plants, which will be part of the first wall and blanket of nuclear fusion reactors, have to sustain the damage produced by the 14 MeV fusion neutrons, temperatures up to 700 °C, and large amounts of He and H coming from transmutation reactions. Main recent research activities focus on developing reduced-activation (RA) steels able to withstand these extreme operation conditions. Oxide dispersion strengthened (ODS) RA ferritic steels (FS) are considered very promising materials, as their use could increase the operating upper temperature limit of RAFS by at least 150 °C [1,2]. Generally, these ODS RAFS are strengthened with a high density of thermally stable Y, Ti-rich oxide nanoparticles homogeneously dispersed in the matrix [1,3]. Their microstructure, having fine grain sizes and high dislocation densities, allow obtaining superior high temperature tensile, creep and fatigue properties in comparison with their non-reinforced counterparts [4–6]. Moreover, their complex microstructure provides a high density of sinks for irradiation induced defects that may lead to lower swelling and increased radiation damage resistance [7–9].

Understanding the irradiation stability of the Y, Ti-rich oxide nanoparticles is crucial to achieve a good performance during the component lifetime in a fusion reactor. In this respect, ion irradiation has become a powerful tool for simulating the particular irradiation conditions present [10]. Radiation damage from primary knock-on atom cascades as well as the effects of He and H transmutation gasses on the irradiated material can both be simulated by using heavy ion irradiation or He and H ion irradiations. However, ion irradiation may have some drawbacks as irradiations carried out in shallow regions may lead to surface effects. Also, the effect of injected ions has to be considered. A relevant issue is the combined exposure to He and displacement damage, which can be investigated by performing dual (either sequential or simultaneous) ion irradiations. For instance, ODS Eurofer showed different radiation behaviours when subjected to single, dual simultaneous, or sequential irradiations, the behaviour also depending on the order of ions [11].

The experimental characterisation of ion irradiations effects aids in understanding main radiation damage processes and contributes to the validation of theoretical models [12]. Positron annihilation spectroscopy (PAS) is one of the techniques employed to characterise defect

* Corresponding author at: Department of Physics, Universidad Carlos III de Madrid, Avda. de la Universidad 30, 28911 Leganes Madrid, Spain.
E-mail address: mscepano@fis.uc3m.es (M. Šćepanović).

https://doi.org/10.1016/j.nme.2020.100790
Received 24 February 2020; Received in revised form 20 June 2020; Accepted 17 August 2020
Available online 21 September 2020

structure evolution under irradiation. PAS, which allows analysing open volume defects, has been successfully applied to study radiation damage in the bulk of steels [13–15]. More recently, some slow PAS investigations have also been accomplished to investigate the evolution of open volume defects in ion-irradiated steels, where the irradiation layer typically extends one to several micrometres from the surface [16–19]. Regarding the microstructural stability of the Y, Ti-rich oxide nanoparticles, many transmission electron microscopy (TEM) and atom probe tomography (APT) studies have reported some nanoparticle evolution under both neutron and ion irradiation. A recent review paper by Wharry et al. analyses and summarises the observed changes (see [20] and references therein). These investigations report different and sometimes opposite variations in the nanoparticle sizes, number densities, chemical compositions, etc., that do not clearly correlate with irradiation doses and temperatures, and are difficult to interpret in terms of one single nucleation and stability mechanism [20]. In order to be able to predict the microstructural changes occurring in ODS steels under irradiation, including the nanoparticle and defect structure evolution, more systematic investigations are needed. One of the problems encountered is the absence of a standard reference ODS batch, which makes difficult to compare investigations among ODS steels that have different chemical compositions, microstructures and nanoparticle features (sizes, number density, composition…). Therefore, it is interesting to extend the experimental database by characterising the effect of different irradiation conditions on the same materials. In previous investigations an ODS Fe14Cr2W0.3Ti steel was characterised after single irradiation with Fe^+ or He^+ ions at different temperatures, and after simultaneous triple irradiation at 600 °C [19,21,22].

In this work, PAS and TEM have been used to investigate the microstructural stability of the same ODS Fe-14Cr-2 W-0.3Ti (wt%) steel and an Fe-14Cr (wt%) model alloy subjected to a dual sequential (He^+, Fe^+) ion irradiation at RT up to 8000 appm He and ~15 dpa Fe with special focus on the nanoparticle stability and the evolution of open volume defects and irradiation induced bubbles.

2. Experimental

Two alloys have been investigated in this work. A model alloy (referred to as Fe14Cr) with nominal composition Fe-14 wt%Cr produced by Goodfellow was vacuum melted, cast and hot rolled. This alloy has an equiaxed grain structure with an average grain size of 100 μm and it is free of dislocations. An ODS steel with nominal composition Fe-14Cr-2W-0.3Ti-0.3Y_2O_3 (wt%), named as ODS, was produced by mechanical alloying of elemental Fe, Cr, W and Ti powders and Y_2O_3 powders in a planetary ball mill under H_2 atmosphere. It was consolidated by hot isostatic pressing (HIP) at 1100 °C and 200 MPa, forged at ~1100 °C and subsequently heat treated at 850 °C for 2 h. Its detailed fabrication process can be found in [23]. The ODS steel has a duplex grain structure with dislocation-free grains < 15 μm and unrecovered grains < 1 μm [23]. Prior to irradiation, samples were cut into approximately 7 × 7 × 0.5 mm^3 pieces, mechanically polished with SiC paper followed by Al_2O_3 until mirror polishing and thermally treated at 800 °C for 2 h in order to remove any possible defects introduced by the polishing process. Heat treatments were carried out in vacuum (~10^{-5} Torr) and samples were furnace-cooled also in vacuum to avoid surface oxidation.

Sequential ion irradiations with He^+ and Fe^+ ions were performed in both materials at room temperature. Samples were first irradiated at the ion implanter at CIEMAT (*Centro de Investigaciones Energéticas, Medioambientales y Tecnológicas*) with 50 keV He^+ ions to a fluence of 10^{16} ions/cm^2 and subsequently irradiated at the Standard multipurpose line of the CMAM (*Centro de Microanálisis de Materiales*) centre with 1 MeV Fe^+ to a fluence of 5.6 × 10^{15} ions/cm^2. The implantation and damage profiles calculated by SRIM (*Stopping and Range of Ions into Matter*) [24] are depicted in Fig. 1 as a function of depth. The maximum damages were estimated using the "Detailed Calculation with full Damage Cascades" mode. Displacement energies for Fe and Cr were 40 eV, leading to 15 dpa (Fe^+) and 0.5 dpa (He^+). Due to the irradiation conditions available for this experiment, the investigations were carried out in regions in which there may be surface effects (~100–300 nm from the surface), see Fig. 1. The Bragg peaks are located at 160 nm from the surface for He ions and 300 nm in the case of Fe ions. The maximum He concentration is 8000 appm (200 nm underneath the surface). It also has to be noted that the calculated maximum of implanted ions is located at 400 nm underneath the surface (Fig. 1). Although the investigated volumes are far from this maximum, there is still a considerable amount of injected Fe ions that could affect the behaviour after irradiation.

Electron transparent lamellae for TEM were obtained by the focused ion beam (FIB) lift-out technique [25]. The instrument was a Zeiss Auriga 40 SEM/FIB equipped with a 30 kV Ga ion gun. Lower ion acceleration voltages (15 to 5 kV) were used in the final preparation stages to minimise surface damage.

Microscopy imaging was performed in various instruments with different microanalysis systems. A Philips CM20 (S)TEM microscope and a JEOL2200MCO prototype microscope were used to characterise the microstructure and secondary phases present in the unirradiated steels. The CM20 was equipped with an energy dispersive spectroscopy (EDS) microanalysis system. The JEOL2200MCO, equipped with an Ω filter, was used for EFTEM acquisition. EFTEM series in the low loss (10–80 eV) energy range were acquired using a 5 eV slit, a 2 eV step and a dwell time of 5 s. The series were drift corrected using the method described in [26]. Elemental maps were extracted using the MMLS (multiple linear least square) method with reference spectra for each element [27]. The irradiated samples were analysed using a JEOL JEM-3000F FEG(S)TEM equipped with a high-angle annular dark field (HAADF) detector and EDS and electron energy loss spectroscopy (EELS) Enfina detectors for microanalysis. The thickness of the samples was determined by EELS using the log-ratio technique [28]. The smallest nanoparticles detected with either of the techniques were about 2 nm in diameter.

The presence of bubbles was investigated by bright-field (BF) TEM using a through-focal technique, being the amount of under/over focus 500 nm. For each sample, five different regions with volumes of the order of 10^{-23} m^3 were analysed. Three of them were centred at ~200 nm from the surface (maximum of the He implantation profile). The fourth region was closer to the surface, centred at ~100 nm and the fifth one was centred deeper into the sample, at ~300 nm.

Slow positron annihilation Doppler Broadening (DB) experiments were performed in NEPOMUC [29] using positrons with energies up to 30 keV. Doppler broadening of the electron–positron annihilation peak at 511 keV gives information of the electron momentum distribution. Annihilation with high-momentum electrons are more probable for delocalised positrons than for trapped positrons, therefore, the narrower the annihilation peak the higher the positron trapping in defects. The observed changes in the width of the annihilation peak at 511 keV as a function of the incident positron energy (correlated with the sample depth) can provide spatial information about the positron trapping in defects. The Doppler broadening of the annihilation peak is usually characterised by the lineshape parameters S and W. The S-parameter is calculated as the ratio between the area of the central portion of the peak and the total area of the peak. The central window used for the S-parameter calculation was 1.632 keV, while the W-parameter was obtained from the higher momentum region and chosen to range from 514.26 to 515.9 keV. The count rate of these measurements was about 300 s^{-1} yielding about 10^7 counts per spectrum.

3. Results and discussion

3.1. Stability of nanoparticles after dual sequential RT ion irradiation

There are two types of submicron sized secondary phases present in

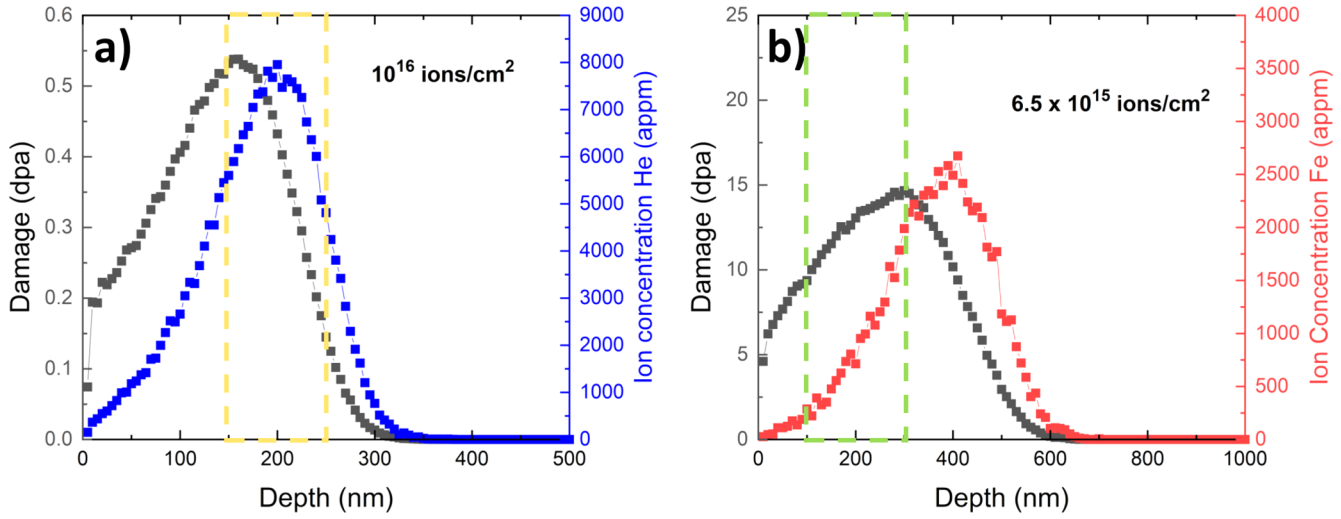

Fig. 1. SRIM profiles of damage and ion concentration for the He/Fe sequential dual irradiation for a) He^+ ions and b) Fe^+ ions. Orange and green rectangles show the main investigated regions for bubbles and nanoparticles, respectively.

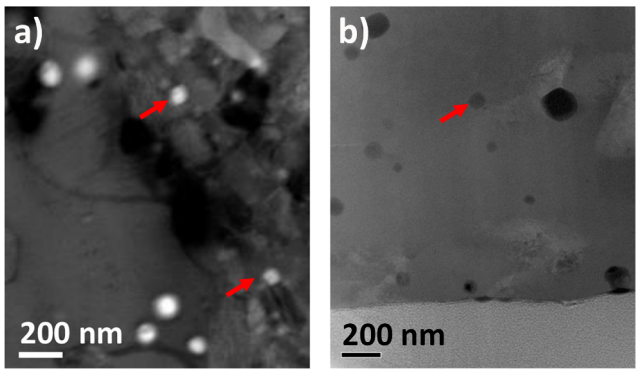

Fig. 2. a) BF-STEM image of the unirradiated and b) HAADF-STEM image of the irradiated ODS steel showing Ti-Cr oxides present in the matrix (some of them marked with arrows).

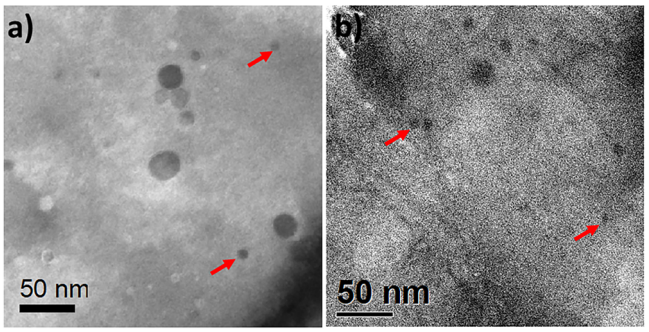

Fig. 3. a) BF-STEM image of the unirradiated and b) HAADF-STEM image of the irradiated ODS steel showing Y-Ti oxides present in the matrix (some of them marked with arrows).

the unirradiated ODS steel, i.e. Ti-Cr oxides with round morphology and sizes ranging from 50 nm to 500 nm (Fig. 2a) and round smaller Y-Ti nano-oxides with sizes below 30 nm (Fig. 3a) [23]. Similar phases have also been found in other ODS steels with akin compositions [30,31]. Both types of secondary phases are still detected in the irradiated ODS steel (Figs. 2b and 3b).

The chemical composition and stability of these secondary phases has been investigated by HAADF-STEM-EDS or EFTEM. For the irradiated ODS steel, the studied regions were centred around 200 nm underneath the irradiated sample surface (13 dpa in the SRIM simulation, see Fig. 1), covering between ~100 nm (9 dpa) and ~300 nm (15 dpa, Bragg peak) from the sample surface. EFTEM and dark-field (DF)-STEM compositional maps showing Y, Ti-rich and Ti, Cr-rich phases in the unirradiated ODS steel are depicted in Figs. 4 and 5a, respectively. Fig. 5b depicts bright-field (BF)-STEM-EDS maps of the larger secondary phases after the irradiation, which maintain their Ti, Cr-rich compositions. STEM-EDS linescans across two nanoparticles in the irradiated steel show similar Y, Ti-rich compositions (Ti and Y signal intensities increase at the location of the nanoparticles), see Fig. 6. In previous atom probe tomography (APT) investigations, Rogozhkin et al showed V and N loss and a slight increase in the Y and Mn concentrations in an ODS-Eurofer steel irradiated at RT with Fe ions to 32 dpa [32]. The concentrations of Y, O and Mn atoms in ODS-Eurofer, of Ti and O atoms in a 13.5Cr–0.3Ti ODS, and of Y atoms in a 13.5Cr ODS also increased after RT Fe or Ti irradiation to 0.8–0.9 dpa [33].

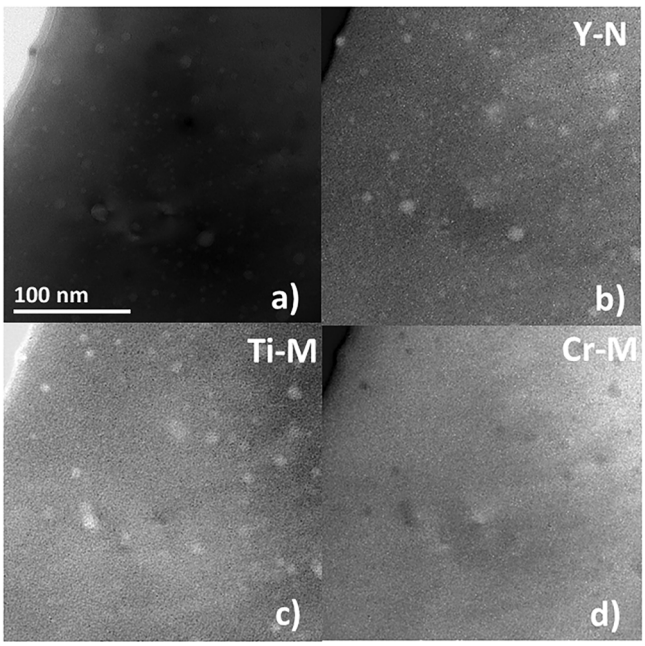

Fig. 4. EFTEM maps showing Y, Ti-rich nanoparticles in the unirradiated ODS steel: a) Elastic image, b) Y-$N_{2,3}$ map, c) Ti-$M_{2,3}$ map, d) Cr-$M_{2,3}$ map. Adapted from [22] with permission from Elsevier.

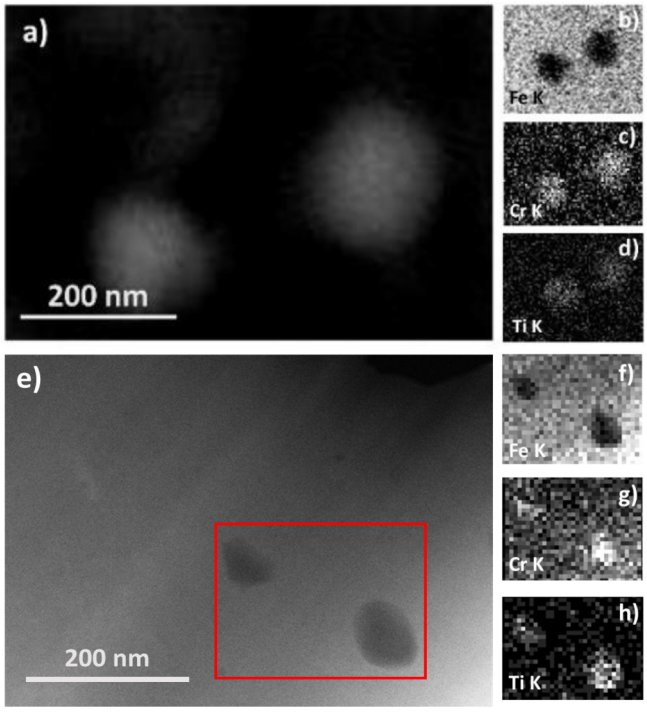

Fig. 5. a) to d): EDS maps showing two Cr-Ti rich precipitates in the unirradiated ODS steel: a) STEM-DF image, b) Fe-K map, c) Cr-K map and d) Ti-K map. e) to h): EDS maps showing two Cr-Ti rich precipitates in the irradiated ODS steel: e) HAADF image, f) Fe-K map, g) Cr-K map and h) Ti-K map.

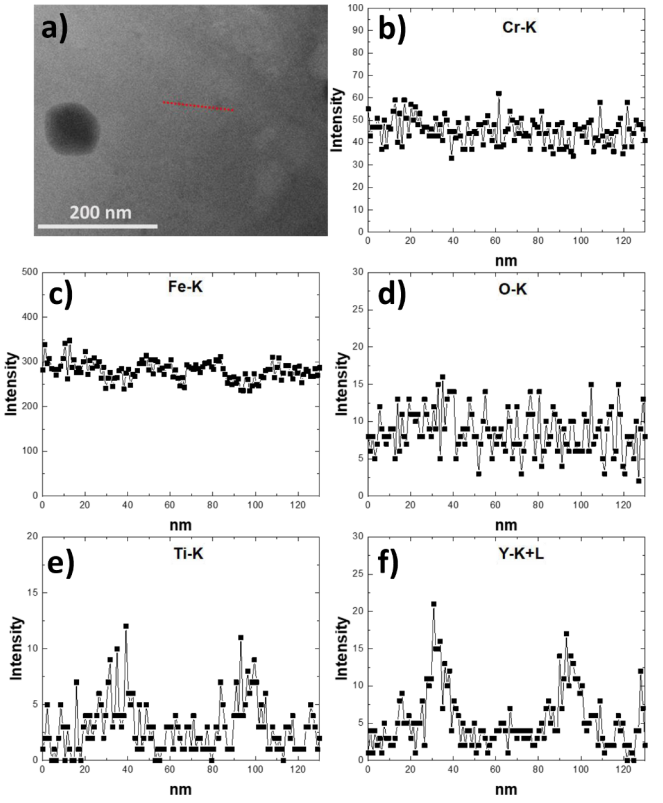

Fig. 6. EDS line-scan of two nanoparticles in the ODS steel after dual sequential He/Fe irradiation at RT: a) HAADF image b) Cr-K signal, c) Fe-K signal, d) O-K signal e) Ti-K signal, and f) Y-K + L signal.

However, investigations accomplished on the same ODS steel as the one studied herein irradiated at −80 °C to 15 dpa with Fe ions showed that the chemical composition of the nanoparticles remains stable [22]. The same behaviour is observed after this dual sequential irradiation, as the chemical composition of the secondary phases seems qualitatively unaltered. Further APT quantitative studies would help to confirm this point.

The nanoparticle size distributions and box plot are presented in Fig. 7. The nanoparticle mean size, 7 ± 4 nm, in the irradiated sample is similar to the one before irradiation (7 ± 5 nm). Some irradiation induced coarsening might be intuited from the histograms (Fig. 7a) the first quartile and median values (Fig. 7b). However, it has to be noted that the measurements had to be carried out using different techniques and the volume that could be investigated after irradiation was much smaller than the one before irradiation.

Existing literature is not conclusive regarding nanoparticle size evolution under low temperature ion irradiation. For instance, Lescoat et al reported complete dissolution of nanoclusters in an 18Cr ODS steel under irradiation at RT to 156 dpa with Au^+ (APT results) although for lower irradiation damages, nanoclusters are still found in the matrix [34]. Certain et al reported nanoparticle dissolution in an 14Cr (W, Ti) ODS steel after Ni^+ irradiation at −75 °C to 100 dpa (APT results). However, EFTEM investigations point to the increase of the average diameter of nanoparticles irradiated at 300 °C to the same dose [35]. Ribis et al also showed nanoparticle size increase at RT after Xe^+ in-situ ion irradiation to 2.5 dpa (TEM results) [36]. However, Kaoumi et al reported that nanoparticles in MA957 are stable after Fe^+ irradiation to 18 dpa at 25 °C (TEM results) in agreement with our results [37].

Histograms from Fig. 7 also show that the small fraction of nanoparticles > 15 nm decreases after the irradiation from 7% to 2%. This would suggest dissolution or shrinkage of the larger nanoparticles. However, it is difficult to make any assumption regarding this point. Large nanoparticles could have been underestimated in the irradiated sample as the magnifications used were optimised to detect the smaller ones.

No significant changes in nanoparticle number densities are detected as compared to the unirradiated steel. Number densities were measured from HAADF images in two regions with volumes of the order of 10^{-21} m^3 being the average density (1.2 ± 0.2) × 10^{22} m^{-3}. This value is similar to the one obtained from EFTEM images in the unirradiated ODS steel that was (1.1 ± 0.2) × 10^{22} m^{-3} [22].

The effect of this dual sequential irradiation on the nanoparticles is almost negligible. Mean sizes and number densities do not vary. TEM histograms only suggest some coarsening of the smallest nanoparticles. Previous APT studies of the same ODS steel after low temperature single Fe ion irradiation showed that nanoparticles < 5 nm were partially dissolving [22]. The same mechanism could be operating here, where incomplete dissolution of nanoparticles below the resolution limit would be contributing to coarsening of the rest.

3.2. TEM characterisation of bubbles induced by dual sequential irradiation

3.2.1. Fe14Cr

The general microstructure of the irradiated model alloy is shown in Fig. 8a. The presence of black dots can be seen homogeneously distributed along the whole depth. As irradiation damage would be located well within the first micron underneath the sample surface, it was assumed that these black dots should be consequence of the Ga-ion damage induced during FIB sample preparation.

Although no evidence of large bubbles was found, the presence of small (< 2 nm) bubbles was observed in all the investigated regions, see examples in Fig. 9. The bubble density is maximum in the regions close to the maximum He concentration (~200 nm from the surface, Fig. 9d–f), ranging from 10 × 10^{23} to 17 × 10^{23} m^{-3} with an average value of (12 ± 3) × 10^{23} m^{-3}. However, there is still a uniform distribution of bubbles at ~100 nm, accounting for diffusion towards the surface (Fig. 9a–c). In the deepest investigated region, around 300 nm depth, a clear bubble density gradient is observed (Fig. 9g–i).

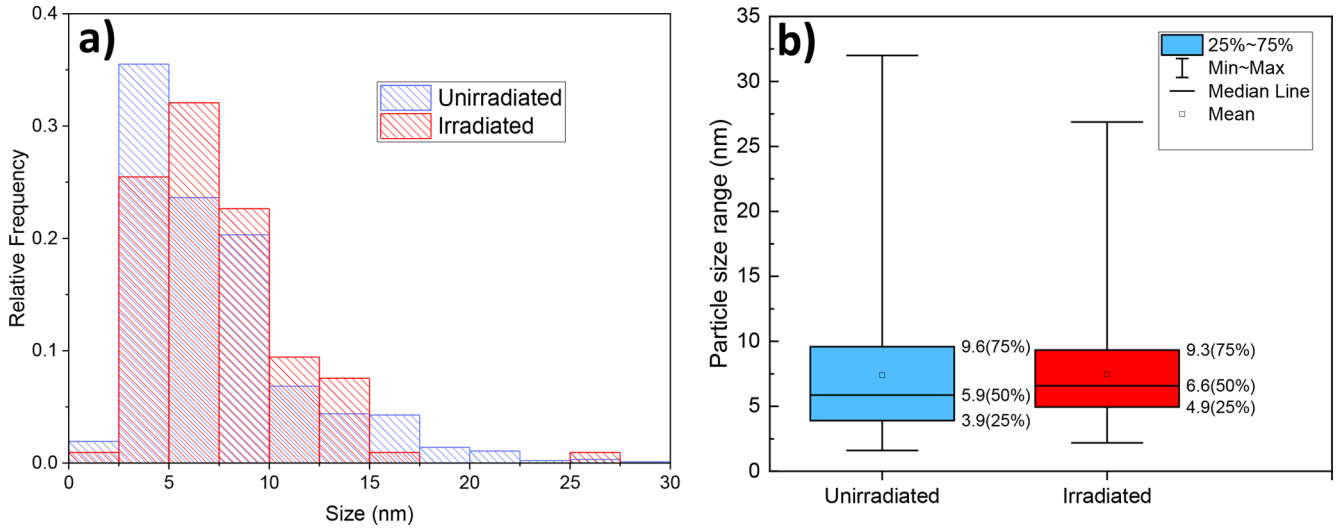

Fig. 7. a) Histogram showing the size distributions of nanoparticles in the ODS steel before and after dual sequential He/Fe irradiation at RT. b) Box plot showing the particle size range before and after dual irradiation.

Closer to the surface, it can be seen that there is still a large amount of bubbles (upper-left corner of Fig. 9g–i). This can be attributed to the fact that Fe^+ irradiation has a Bragg peak at ~300 nm thus creating a large amount of vacancies that could coalesce or act as points of He-bubble nucleation at that zone. The density of bubbles clearly decreases towards deeper regions (lower-right corner of Fig. 9g–i), in agreement with the sharp increase in the ion concentration predicted by SRIM.

The size of the bubbles was measured in the three regions centred at ~200 nm from the surface. Fig. 10a shows the size distribution of these small bubbles, which are < 2 nm having mean sizes of 1.2 ± 0.3 nm. This mean size is comparable to the one found for a Eurofer steel irradiated with Fe^{3+} and He^+ at 330 °C to a dose of 26 dpa and 450 appm, respectively, where the mean bubble size was 1.3 nm, being the bubble number density slightly lower (2×10^{23} m^{-3}) [38]. The measured sizes are slightly smaller to those observed for Fe5%Cr irradiated with 100 dpa Fe^+ and 2500 appm He^+ at 500 °C (2.2 nm). It has to be taken into account that the irradiations performed in the present work were accomplished at RT and to lower doses, although the amount of He implanted hereby is much larger (8000 appm) [39]. The bubble sizes are lower, and the bubble number densities higher after this dual sequential He/Fe irradiation when compared to results obtained from the same Fe14Cr model alloy irradiated with He^+ ions to 4700 appm at 400 °C, 1.4 nm and 4×10^{23} m^{-3} respectively [19]. This could be related to the lower irradiation temperature and larger concentration of the He^+ ions introduced by the dual irradiation, along with the larger amount of vacancy-type defects induced by the irradiation.

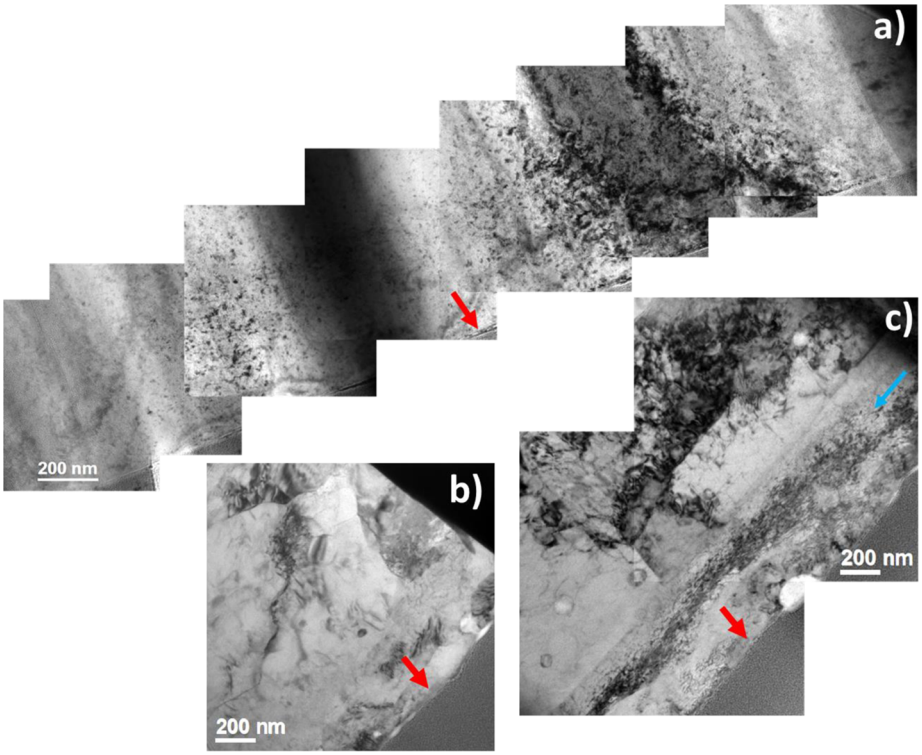

Fig. 8. General BF images after sequential He/Fe ion irradiation at RT of: a) the FIB-ed Fe14Cr model alloy. b) the ODS steel and c) the ODS steel after tilting by 10°. Red arrows indicate the sample surface. A blue arrow marks the irradiation induced defect fringe.

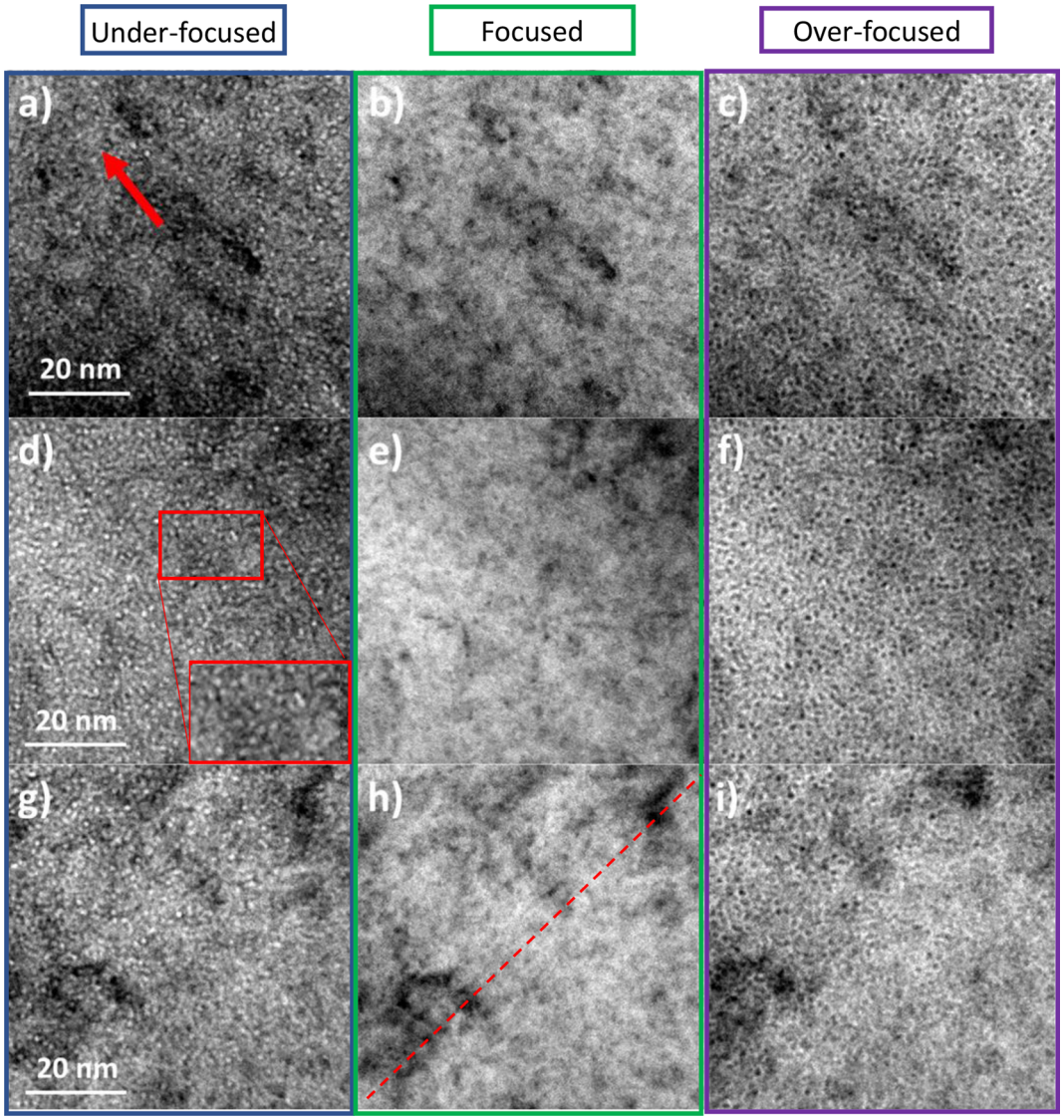

Fig. 9. Through-focal series of three regions in the Fe14Cr alloy after sequential He/Fe ion irradiation at RT. BF images a) to c) show a region ~100 nm away from the surface, where the arrow points in the direction towards the surface. Images d) to f) correspond to a region inside the bubble fringe, ~200 nm away from the surface, where the inset in d) shows magnified bubbles. Images g) to i) show a region ~300 nm away from the surface where a clear bubble density gradient can be observed. The dashed line in h) separates regions with different bubble density, with higher density in the top left and lower in the bottom right.

3.2.2. ODS

Fig. 8b shows a general image of the microstructure of the irradiated ODS steel where no defects or bubble fringe are observed under these orientation conditions. However, after tilting the sample by an angle of 10° (see Fig. 8c), a defect fringe is revealed between ~200 and 400 nm, coinciding with the location of the Bragg peak simulated by SRIM. At

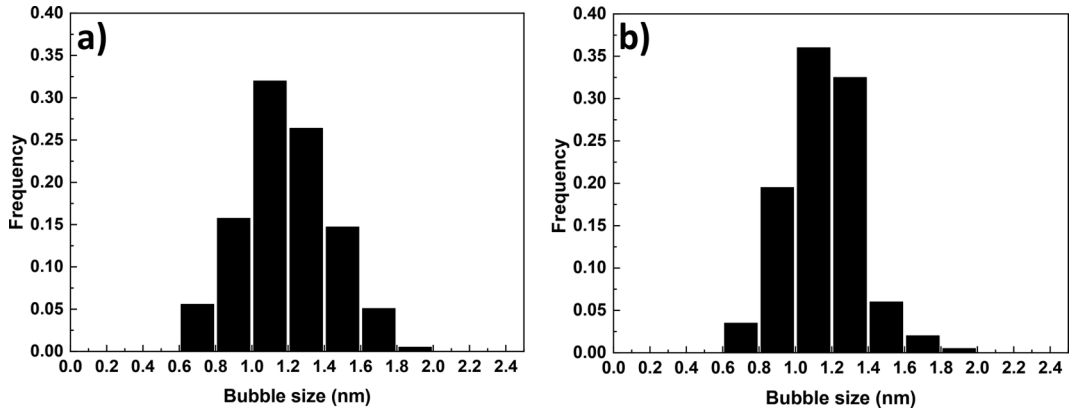

Fig. 10. Size distribution of bubbles measured in a) Fe14Cr alloy and b) ODS steel after sequential He/Fe ion irradiation at RT.

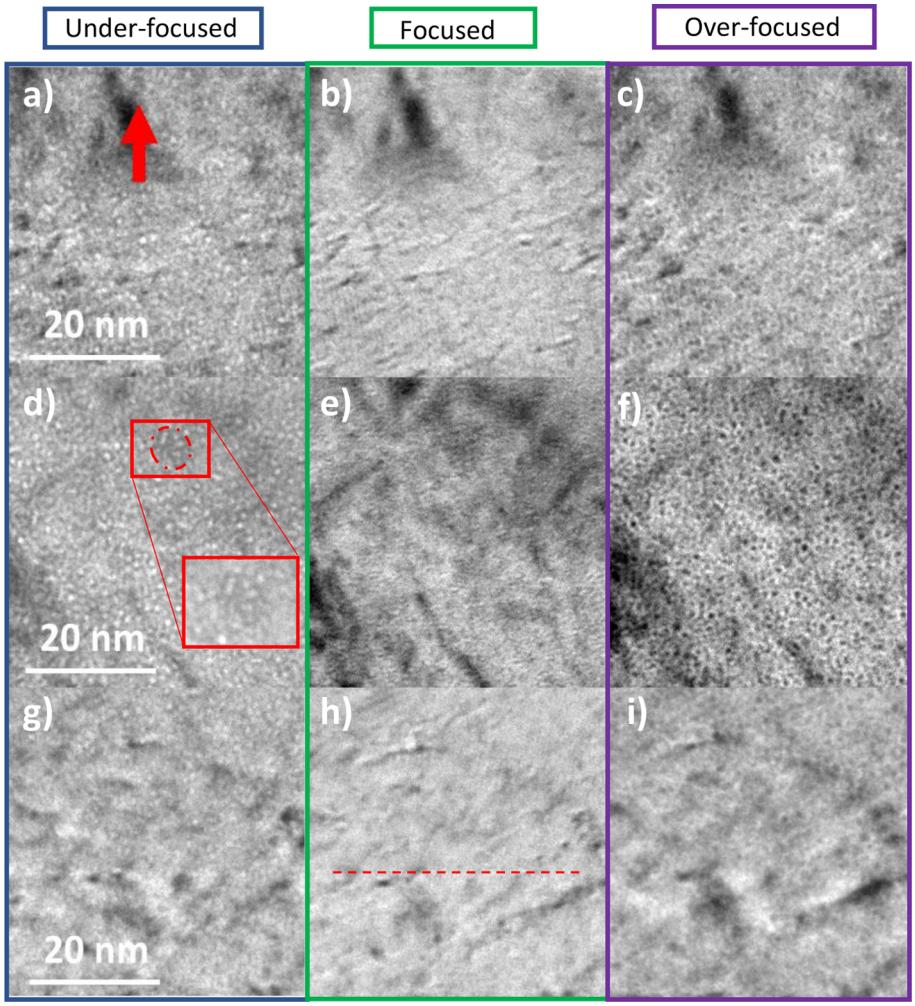

Fig. 11. Through-focal series of three regions in the sequential He/Fe irradiated ODS alloy. BF images a) to c) show a region ~100 nm away from the surface, where the arrow points in the direction towards the surface. Images d) to f) depict a region inside the bubble fringe, ~200 nm away from the surface. The corresponding inset shows bubbles attached to what appears to be a nanoparticle, which is highlighted by a dashed line. Images g) to i) show a region ~300 nm away from the surface, where the dashed line in h) separates regions having different bubble density, with higher density on top and lower on the bottom.

higher magnifications, small bubbles (< 2 nm) are observed out of focus (Fig. 11). As in the case of the model alloy, these bubbles were investigated in the zone of maximum He concentration, closer to the surface and in the zone of maximum damage. Close to the surface, at ~100 nm depth (Fig. 11a–c) bubbles appear homogeneous, hinting to the diffusion of He towards the surface of the sample. At the location of maximum He concentration, the bubbles are uniformly dispersed throughout the matrix, as can be seen in Fig. 11d–f. In the innermost region investigated (~300 nm depth, Fig. 11g–i) bubbles are still observed but, likewise in the model alloy, a bubble gradient is noticed.

Most bubbles were found uniformly dispersed in the matrix. Only some bubbles were observed to be attached to nanoparticles. Number densities calculated for the region of maximum He concentration range from 7.2×10^{23} to 11×10^{23} m^{-3}, with an average value of $(9 \pm 2) \times 10^{23}$ m^{-3}.

Sizes of bubbles were measured in regions around the maximum He concentration. Their size distribution is shown in Fig. 10b, with a mean size of 1.2 ± 0.2 nm. This mean size is similar to the one observed for the Fe14Cr alloy irradiated under the same conditions. The number density in the region of maximum He concentration appears to be lower for this sample than for the model alloy. This could be due to the sizes of bubbles being below the detection limit, hence the number density would appear to be lower. This behaviour was also observed by Lu et al. after a single He^+ irradiation at 400 °C to a fluence of 1×10^{17} ions/cm^2 of 14Cr ODS steel and EUROFER 97 steel [40].

3.3. Characterisation of open volume defects by PAS

Fig. 12 shows the lineshape S and W parameters as a function of the incident positron energy for the Fe14Cr model alloy after the sequential He/Fe irradiation, together with the results for the unirradiated alloy and for the same model alloy after single He^+ and Fe^+ irradiations [19]. The S-parameter of the well-annealed unirradiated model alloy is reflecting the absence of open volume defects, as it shows the characteristic steep decrease from annihilations occurring either at the surface or the bulk in defect-free samples [41]. The S-parameter values clearly increase after the single irradiations. As it can be seen, the effect of the single He^+ irradiation is much weaker than the changes induced by the single Fe^+ irradiation. Fig. 12 also shows that for the He^+ irradiation the maximum differences with respect to the unirradiated values shift to lower incident positron energies, indicating that irradiation induced defects are closer to the surface. The S-parameter of the sequential He/Fe irradiation is considerably larger than the one for the single He^+ irradiation, approaching the S value after the single Fe^+ irradiation. This is consistent with the larger amount of vacancy-type defects created by the subsequent Fe^+ irradiation. However, it can be

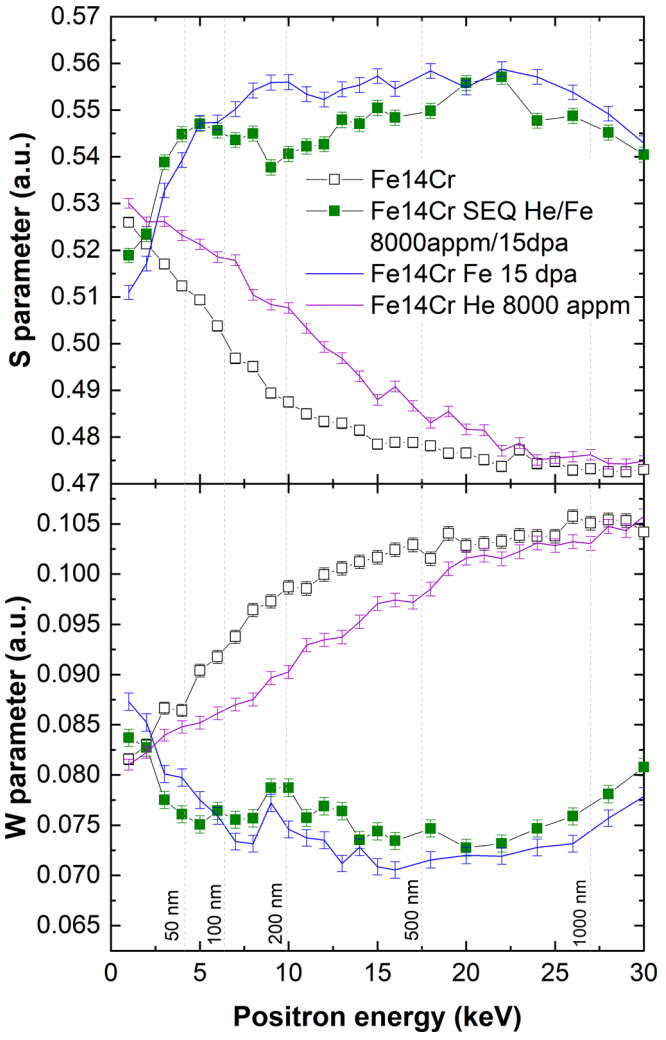

Fig. 12. a) S-parameter and b) W-parameter for the well-annealed Fe14Cr model alloy before and after the dual sequential He/Fe irradiation at RT as a function of incident positron energy. Results after single Fe^+ and He^+ irradiations from ref [19] are also given for comparison.

seen that in the energy range 5–20 keV the S-parameter for the dual sequential irradiation is lower than for the single Fe^+ irradiation, with a local minimum occurring at 9 keV. This would suggest that the type/size of positron traps detected within this energy range (the one for which He irradiation effects are evident) has changed with respect to the single Fe^+ irradiation. The incident positron energy at the local minimum (9 keV) corresponds to a mean implantation depth of ~170 nm, which is very close to the calculated maximum He concentration depth (~200 nm) as seen in Fig. 1, also coinciding with the regions with higher bubble density observed by TEM. While the S-parameter increase at 9 keV for the single Fe^+ irradiation is 17.5% higher than for the unirradiated bulk value, this difference is 13.6% for the sequential irradiation. A possible explanation would be the coarsening of pre-existing He-vacancy complexes created during the He^+ irradiation due to the subsequent Fe^+ irradiation, or migration of the implanted He into the newly formed open-volume defects. In any case, the characteristics of these He-vacancy complexes would be different than vacancy clusters produced by the single Fe^+ irradiation.

These results are consistent with previous works. Troev et al. calculated that the lifetime of positron in α-Fe containing He decreases monotonically depending on the He introduction in the iron vacancy-cluster [42]. This was experimentally shown by Ramachandran et al. by irradiating a RAFM steel with 130 keV He ions to fluences of 5×10^{14} and 1×10^{16} ions/cm^2 and isochronally annealing them from RT to 973 K [43]. Sabelova et al. showed that for a He^+ irradiated Fe12Cr alloy to a fluence of 1.25×10^{18} ions/cm^2 the S-parameter is higher in the zone of maximum damage compared to the zone of maximum He concentration [44]. Kögler et al. observed that the S-parameter of pure Fe after simultaneous Fe/He irradiation is lower than in the case of a single Fe^+ irradiation, attributing that to the presence of He in the vacancy clusters [45]. Lu et al. showed that for a FeCrNi austenitic steel irradiated with He ions to fluences of the order of 10^{16} ions/cm^2 at RT, He-vacancy complexes formed in zone of maximum concentration of He, which prevented the increase of the S-parameter at higher damage dose [46]. A similar behaviour was observed in the work of García-Cortés et al, where a Fe14Cr model alloy was irradiated sequentially at RT, first with Fe ions and then with He ions [18]. When comparing the results obtained hereby with those from [18], the effect of the different order of ions in sequential irradiations can be noted, with the S parameter of the Fe/He sequence being much lower than in the case described here. Hence, while in the sample pre-irradiated with He some of the He ions get trapped in the zone of maximum He concentration, in the sample post-irradiated with He, it appears that all of the He ions are being trapped by the Fe^+ irradiation induced open-volume defects increasing the electron density in the traps, thus further lowering the S-parameter.

At energies > 20 keV the S-parameter of the sequential irradiation is very similar to the single Fe^+ irradiated, with slightly lower values that could indicate the remaining contribution of the shallower He-related traps. At 30 keV the S-parameter of the sequential irradiation has the same value as the S-parameter of the single Fe^+ irradiation, suggesting that at this mean depth there are no more detectable positron traps related to He. These results also appear to agree with TEM findings, where the bubble density largely decreases towards regions deeper than 300 nm.

The S and W-parameter values for the ODS steel in unirradiated state as well as after the sequential He/Fe, single Fe^+ and single He^+ irradiations are shown in Fig. 13. The S-parameter of the unirradiated ODS alloy has a flat profile indicating that it already contains uniformly dispersed open-volume positron traps, in agreement with the findings performed by P. Parente on the same unirradiated ODS steel [16]. The sequential irradiation in the ODS steel induces less observable changes compared to the Fe14Cr model alloy, similarly to what happens for the single He^+ and single Fe^+ irradiations [19]. The much higher difference in the S-parameter values before and after irradiation obtained for the model alloy compared to the ODS steel is due to the fact that the model alloy contains initially almost no vacancy traps (particles, dislocations, etc), leading to a higher concentration and/or larger size of vacancy clusters forming under the irradiation. The S-parameter values for the sequential irradiation are very similar to the ones measured for the single Fe^+ irradiation (a maximum increase of ~6% with respect to the bulk of the unirradiated sample), although they seem to be slightly lower in the energy range 4–16 keV. This could be attributed to the association of the open-volume defects with the implanted He ions. However, unlike in the previously discussed model alloy, this difference is quite small and the S-parameter in the case of the ODS sample does not show a clear local minimum around the depth of maximum implanted He The small homogeneously dispersed Y-Ti nanoparticles present in the ODS steel would inhibit the growth of vacancy clusters, thus lowering the percentage increase of S-parameter values after the single Fe^+ irradiation compared to the model alloy (6% in ODS compared to 18% in Fe14Cr). These results would agree with the TEM analyses previously discussed, which also suggest that there are less

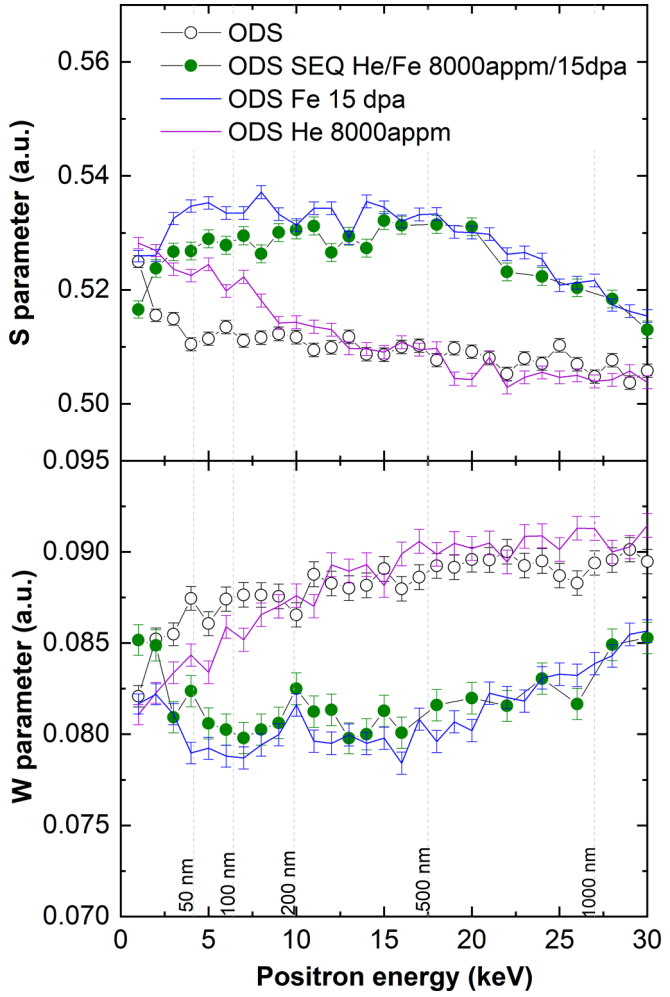

Fig. 13. Doppler Broadening results for ODS steel before and after the sequential He/Fe irradiation at RT. Results after single Fe^+ and He^+ irradiations from ref [19] are also given for comparison. a) S-parameter and b) W-parameter.

visible bubbles compared to the model alloy. In the sequential irradiation, the effect of the implanted He^+ followed by the Fe^+ irradiation is similar to the one observed in the model alloy, decreasing the annihilations with low momentum electrons in the energy range where He

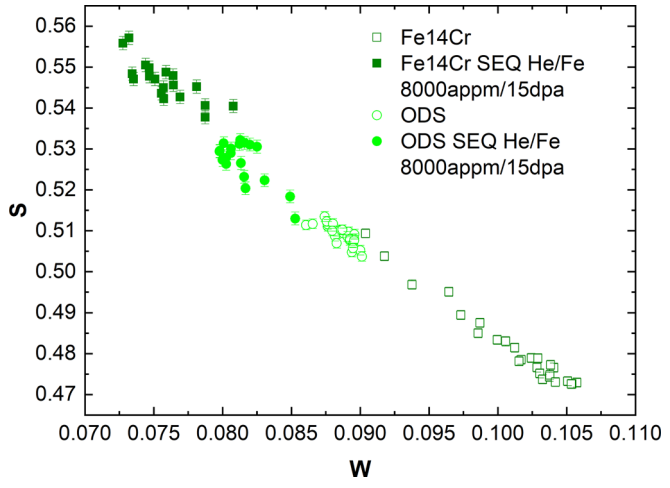

Fig. 14. S/W plot for the model alloy and the ODS steel before and after the sequential irradiations.

effects could be detected. This suggests that similarly to what occurred for the sequential irradiation in the Fe14Cr model alloy, He tends to associate with open-volume defects created or enlarged by the Fe^+ irradiation, albeit the effect in the S-depth profile is not as visible due to irradiation induced damage being much lower in the ODS steel.

Fig. 14 shows the S/W plot for the Fe14Cr model alloy and the ODS steel after sequential irradiations along with their unirradiated counterparts. The S/W points corresponding to irradiated alloys follow the same trend as those for unirradiated samples. No clear effect of He-vacancy complexes was observed, as the data points corresponding to the energy range in which He concentration is maximum (7–12 keV) are not grouped in any way.

4. Conclusions

The effects of a sequential dual He/Fe irradiation performed at RT on a model Fe14Cr alloy and an ODS Fe14Cr2W0.3Ti ferritic steel were investigated by TEM and PAS. The results are summarised below:

- The stability of the nanoparticles present in the ODS steel was investigated by TEM. The nanoparticles appear to be quite stable. Their chemical compositions are qualitatively unaltered. Nanoparticle mean sizes and number densities remain similar, although size distribution histograms point to some coarsening.
- TEM investigations of irradiation induced bubbles were performed on both alloys. Only very small bubbles (< 2 nm) were detected in both materials, the bubble number density clearly decreasing towards regions deeper than ~300 nm in agreement with the simulated SRIM profile. The majority of the bubbles are observed dispersed in the ferritic matrix. Although for these irradiation conditions visible bubble sizes are similar for the ODS steel compared to the model alloy, the lower visible number density measured for the ODS steel as compared to the model alloy would point to bubbles being below the detection limit in the ODS steel.
- The DB PAS investigations performed on the model alloy suggest association of He with the newly formed vacancy-type defects introduced by the subsequent Fe^+ irradiation either by coarsening of the He-vacancy complexes or migration of pre-implanted He atoms. In the case of the ODS steel, PAS analyses show that the nanoparticle dispersion, as well as the other vacancy traps present in its complex microstructure, help reducing the irradiation induced damage. The He trapping effect in the newly formed open-volume defects is still present, although not as visible compared to model alloys.

CRediT authorship contribution statement

M. Šćepanović: Investigation, Writing - original draft, Writing - review & editing. **T. Leguey:** Investigation, Writing - original draft, Writing - review & editing, Resources, Supervision. **I. García-Cortés:** Investigation, Resources. **F.J. Sánchez:** Investigation, Resources. **C. Hugenschmidt:** Investigation, Resources, Writing - review & editing. **M.A. Auger:** Investigation, Resources. **V. Castro:** Investigation, Writing - original draft, Writing - review & editing, Resources, Supervision.

Declaration of Competing Interest

The authors declare that they have no known competing financial interests or personal relationships that could have appeared to influence the work reported in this paper.

Acknowledgements

This investigation has been supported by the Ministerio de Economía y Competitividad (project ENE2015-70300-C3-2-R) and the Comunidad de Madrid through the program TECHNOFUSIÓN-III

(S2018/EMT-4437), Talento-CAM (2017-T1/IND-5439) and the project ENE2016-76755_R. The authors gratefully acknowledge the financial support provided by FRM II to perform slow positron annihilation measurements at the Heinz Maier-Leibnitz Zentrum (MLZ), Garching, Germany. EFTEM maps were obtained using funding from the European Union Seventh Framework Programme under Grant Agreement 312483 - ESTEEM2 (Integrated Infrastructure Initiative – I3). Funding from Comunidad Autónoma de Madrid-Spain (2017-T1/IND-5439) is gratefully acknowledged. The authors also acknowledge the support provided by CMAM and CIEMAT facilities, the Department of Materials at the University of Oxford (UK) and the Centro Nacional de Microscopía Electrónica (Madrid, Spain).

References

[1] J.L. Boutard, A. Alamo, R. Lindau, M. Rieth, Fissile core and Tritium-Breeding Blanket: structural materials and their requirements, Comptes. Rendus. Phys. 9 (2008) 287–302, https://doi.org/10.1016/j.crhy.2007.11.004.

[2] R.J. Kurtz, A. Alamo, E. Lucon, Q. Huang, S. Jitsukawa, A. Kimura, R.L. Klueh, G.R. Odette, C. Petersen, M.A. Sokolov, P. Spätig, J.W. Rensman, Recent progress toward development of reduced activation ferritic/martensitic steels for fusion structural applications, J. Nucl. Mater. 386–388 (2009) 411–417, https://doi.org/10.1016/j.jnucmat.2008.12.323.

[3] C.A. Williams, P. Unifantowicz, N. Baluc, G.D.W. Smith, E.A. Marquis, The formation and evolution of oxide particles in oxide-dispersion- strengthened ferritic steels during processing, Acta Mater. 61 (2013) 2219–2235, https://doi.org/10.1016/j.actamat.2012.12.042.

[4] H.Y. Fu, T. Nagasaka, T. Muroga, A. Kimura, J.M. Chen, Microstructural characterization of a diffusion-bonded joint for 9Cr-ODS and JLF-1 reduced activation ferritic/martensitic steels, Fusion Eng. Des. 89 (2014) 1658–1663, https://doi.org/10.1016/J.FUSENGDES.2014.02.055.

[5] L. Tan, L.L. Snead, Y. Katoh, Development of new generation reduced activation ferritic-martensitic steels for advanced fusion reactors, J. Nucl. Mater. 478 (2016) 42–49, https://doi.org/10.1016/j.jnucmat.2016.05.037.

[6] P. Song, D. Morrall, Z. Zhang, K. Yabuuchi, A. Kimura, Radiation response of ODS ferritic steels with different oxide particles under ion-irradiation at 550 °C, J. Nucl. Mater. 502 (2018) 76–85, https://doi.org/10.1016/J.JNUCMAT.2018.02.007.

[7] R.L. Klueh, D.R. Harries, High-chromium ferritic and martensitic steels for nuclear applications, ASTM International, 2001.

[8] C. Hin, B.D. Wirth, Formation of Y2O3 nanoclusters in nano-structured ferritic alloys: Modeling of precipitation kinetics and yield strength, J. Nucl. Mater. 402 (2010) 30–37, https://doi.org/10.1016/J.JNUCMAT.2010.04.020.

[9] S. Santra, S. Amirthapandian, S. Balaji, B.K. Panigrahi, Y. Serruys, C. Robertson, Ion irradiation stability of oxide nano-particles in ODS alloys: TEM studies, J. Nucl. Mater. 528 (2020) 151861, https://doi.org/10.1016/J.JNUCMAT.2019.151861.

[10] G.S. Was, Z. Jiao, E. Getto, K. Sun, A.M. Monterrosa, S.A. Maloy, O. Anderoglu, B.H. Sencer, M. Hackett, Emulation of reactor irradiation damage using ion beams, Scr. Mater. 88 (2014) 33–36, https://doi.org/10.1016/J.SCRIPTAMAT.2014.06.003.

[11] C. Heintze, F. Bergner, M. Hernández-Mayoral, R. Kögler, G. Müller, A. Ulbricht, Irradiation hardening of Fe–9Cr-based alloys and ODS Eurofer: effect of helium implantation and iron-ion irradiation at 300 °C including sequence effects, J. Nucl. Mater. 470 (2016) 258–267, https://doi.org/10.1016/J.JNUCMAT.2015.12.041.

[12] Y. Dai, G.R. Odette, T. Yamamoto, The effects of helium in irradiated structural alloys, 1st ed., Elsevier Inc., 2012. doi:10.1016/B978-0-08-056033-5.00006-9.

[13] R. Pareja, N. de Diego, R.M. De la Cruz, Postirradiation recovery of a reactor pressure vessel steel investigated by positron annihilation and microhardness measurements, Nucl. Technol. 104 (1993) 52–63, https://doi.org/10.13182/NT93-A34869.

[14] R.M. Hengstler-Eger, P. Baldo, L. Beck, J. Dorner, K. Ertl, P.B. Hoffmann, C. Hugenschmidt, M.A. Kirk, W. Petry, P. Pikart, A. Rempel, Heavy ion irradiation induced dislocation loops in AREVA's M5® alloy, J. Nucl. Mater. 423 (2012) 170–182, https://doi.org/10.1016/J.JNUCMAT.2012.01.002.

[15] V. Sabelová, V. Kršjak, J. Kuriplach, Y. Dai, V. Slugeň, Coincidence Doppler broadening study of Eurofer 97 irradiated in spallation environment, J. Nucl. Mater. 458 (2015) 350–354, https://doi.org/10.1016/J.JNUCMAT.2014.12.053.

[16] P. Parente, T. Leguey, V. De Castro, T. Gigl, M. Reiner, C. Hugenschmidt, R. Pareja, Characterization of ion-irradiated ODS Fe-Cr alloys by doppler broadening spectroscopy using a positron beam, J. Nucl. Mater. 464 (2015) 140–146, https://doi.org/10.1016/j.jnucmat.2015.04.033.

[17] S. Pecko, C. Heintze, F. Bergner, W. Anwand, V. Slugeň, Fe2+ ion irradiated JRQ steel investigated by nanoindentation and slow-positron Doppler broadening spectroscopy, Nucl. Instrum. Methods Phys. Res. Sect. B Beam Interact. Mater. Atoms. 415 (2018) 1–8, https://doi.org/10.1016/J.NIMB.2017.11.002.

[18] I. García-Cortés, T. Leguey, F.J. Sánchez, A. Maira, A. Moroño, P. Muñoz, M. Scepanovic, J.F. Marco, Study of damage in binary Fe85Cr15 alloys irradiated by ions and the effect of an external magnetic field during irradiation, J. Nucl. Mater. 517 (2019) 138–147, https://doi.org/10.1016/J.JNUCMAT.2019.02.009.

[19] M. Šćepanović, V. de Castro, I. García-Cortés, F.J. Sánchez, T. Gigl, C. Hugenschmidt, T. Leguey, Characterisation of open volume defects in Fe–Cr and ODS Fe–Cr alloys after He+ and Fe+ ion irradiations, J. Nucl. Mater. (2020) 152230, https://doi.org/10.1016/j.jnucmat.2020.152230.

[20] J.P. Wharry, M.J. Swenson, K.H. Yano, A review of the irradiation evolution of dispersed oxide nanoparticles in the b.c.c. Fe-Cr system: current understanding and future directions, J. Nucl. Mater. 486 (2017) 11–20, https://doi.org/10.1016/j.jnucmat.2017.01.009.

[21] M. Šćepanović, V. de Castro, T. Leguey, M.A. Auger, S. Lozano-Perez, R. Pareja, Microstructural stability of ODS Fe-14Cr (-2W-0.3Ti) steels after simultaneous triple irradiation, Nucl. Mater. Energy 9 (2016) 490–495, https://doi.org/10.1016/j.nme.2016.08.001.

[22] M. Šćepanović, T. Leguey, M.A. Auger, S. Lozano-Perez, D.E.J. Armstrong, I. García-Cortés, V. de Castro, Characterisation of ODS Fe-14Cr-2W-0.3Ti before and after high temperature triple and low temperature single ion irradiations, Mater. Charact. 136 (2018), https://doi.org/10.1016/j.matchar.2017.12.025.

[23] M.A. Auger, V. de Castro, T. Leguey, M.A. Monge, A. Muñoz, R. Pareja, Microstructure and tensile properties of oxide dispersion strengthened Fe–14Cr–0.3Y2O3 and Fe–14Cr–2W–0.3Ti–0.3Y2O3, J. Nucl. Mater. 442 (2013) S142–S147, https://doi.org/10.1016/j.jnucmat.2012.11.001.

[24] J.F. Ziegler, M.D. Ziegler, J.P. Biersack, SRIM – the stopping and range of ions in matter (2010), Nucl. Instrum. Methods Phys. Res. Sect. B Beam Interact. Mater. Atoms. 268 (2010) 1818–1823. doi:10.1016/J.NIMB.2010.02.091.

[25] S. Lozano-Perez, A guide on FIB preparation of samples containing stress corrosion crack tips for TEM and atom-probe analysis, Micron 39 (2008) 320–328, https://doi.org/10.1016/J.MICRON.2007.12.003.

[26] B. Schaffer, W. Grogger, G. Kothleitner, Automated spatial drift correction for EFTEM image series, Ultramicroscopy 102 (2004) 27–36, https://doi.org/10.1016/j.ultramic.2004.08.003.

[27] D.B. Williams, C.B. Carter, Transmission Electron Microscopy, Springer US, 2009. doi:10.1007/978-0-387-76501-3.

[28] T. Malis, S.C. Cheng, R.F. Egerton, EELS log-ratio technique for specimen-thickness measurement in the TEM, J. Electron. Microsc. Tech. 8 (1988) 193–200, https://doi.org/10.1002/jemt.1060080206.

[29] C. Hugenschmidt, C. Piochacz, NEPOMUC: neutron induced positron source Munich, J. Large-Scale Res. Facil. JLSRF. 1 (2015) A22, https://doi.org/10.17815/jlsrf-1-49.

[30] J. Macías-Delgado, T. Leguey, V. de Castro, Effect of hot cross rolling on the microstructure and mechanical properties of an Fe-14Cr ODS ferritic steel, Mater. Sci. Eng., A 711 (2018) 448–459, https://doi.org/10.1016/j.msea.2017.11.067.

[31] H. Sakasegawa, L. Chaffron, F. Legendre, L. Boulanger, T. Cozzika, M. Brocq, Y. de Carlan, Correlation between chemical composition and size of very small oxide particles in the MA957 ODS ferritic alloy, J. Nucl. Mater. 384 (2009) 115–118, https://doi.org/10.1016/j.jnucmat.2008.11.001.

[32] S.V. Rogozhkin, N.N. Orlov, A.A. Aleev, A.G. Zaluzhnyi, M.A. Kozodaev, R.P. Kuibeda, T.V. Kulevoy, A.A. Nikitin, B.B. Chalykh, R. Lindau, A. Möslang, P. Vladimirov, Nanostructure evolution in ODS Eurofer steel under irradiation up to 32 dpa, Phys. Met. Metallogr. 116 (2015) 72–78, https://doi.org/10.1134/S0031918X15010093.

[33] S.V. Rogozhkin, A. Bogachev, O. Korchuganova, A. Nikitin, N. Orlov, A. Aleev, A. Zaluzhnyi, M. Kozodaev, T. Kulevoy, B. Chalykh, R. Lindau, J. Hoffmann, A. Moslang, P. Vladimirov, M. Klimenkov, M. Heilmaier, J. Wagner, S. Seils, Nanostructure evolution in ODS steels under ion irradiation, Nucl. Mater. Energy 9 (2016) 66–74, https://doi.org/10.1016/j.nme.2016.06.011.

[34] M.L. Lescoat, J. Ribis, Y. Chen, E.A. Marquis, E. Bordas, P. Trocellier, Y. Serruys, A. Gentils, O. Kaïtasov, Y. De Carlan, A. Legris, Radiation-induced Ostwald ripening in oxide dispersion strengthened ferritic steels irradiated at high ion dose, Acta Mater. 78 (2014) 328–340, https://doi.org/10.1016/j.actamat.2014.06.060.

[35] A. Certain, S. Kuchibhatla, V. Shutthanandan, D.T. Hoelzer, T.R. Allen, Radiation stability of nanoclusters in nano-structured oxide dispersion strengthened (ODS) steels, J. Nucl. Mater. 434 (2013) 311–321, https://doi.org/10.1016/j.jnucmat.2012.11.021.

[36] J. Ribis, M.L. Lescoat, Y. De Carlan, J.M. Costantini, I. Monnet, T. Cozzika, F. Delabrouille, J. Malaplate, Stability of nano-oxides upon heavy ion irradiation of an ODS material, J. Nucl. Mater., North-Holland (2011) 262–265, https://doi.org/10.1016/j.jnucmat.2010.12.068.

[37] D. Kaoumi, A. Motta, M. Kirk, Characterization and in-situ ion-irradiation of MA957 ODS steel, Trans. Am. Nucl. Soc. 98 (2008) 1113–1114.

[38] B. Kaiser, C. Dethloff, E. Gaganidze, D. Brimbal, M. Payet, P. Trocellier, L. Beck, J. Aktaa, TEM study and modeling of bubble formation in dual-beam He+/Fe3+ ion irradiated EUROFER97, J. Nucl. Mater. 484 (2017) 59–67, https://doi.org/10.1016/J.JNUCMAT.2016.11.014.

[39] D. Brimbal, E. Meslin, J. Henry, B. Décamps, A. Barbu, He and Cr effects on radiation damage formation in ion-irradiated pure iron and Fe-5.40 wt.% Cr: A transmission electron microscopy study, Acta Mater. 61 (2013) 4757–4764, https://doi.org/10.1016/j.actamat.2013.04.070.

[40] C. Lu, Z. Lu, R. Xie, C. Liu, L. Wang, Microstructure of a 14Cr-ODS ferritic steel before and after helium ion implantation, J. Nucl. Mater. 455 (2014) 366–370, https://doi.org/10.1016/J.JNUCMAT.2014.06.065.

[41] K.G. Lynn, D.M. Chen, B. Nielsen, R. Pareja, S. Myers, Variable-energy positron-beam studies of Ni implanted with He, Phys. Rev. B 34 (1986) 1449–1458, https://

doi.org/10.1103/PhysRevB.34.1449.
[42] T. Troev, E. Popov, P. Staikov, N. Nankov, Positron lifetime studies of defects in α-Fe containing helium, Phys. Status Solidi Curr. Top. Solid State Phys. 6 (2009) 2373–2375, https://doi.org/10.1002/pssc.200982129.
[43] R. Ramachandran, C. David, R. Rajaraman, B.K. Panigrahi, G. Amarendra, C. David, R. Rajaraman, B.K. Panigrahi, G. Amarendra, Evolution , migration and clustering of helium- vacancy complexes in RAFM steel- depth resolved positron annihilation Doppler broadening study, 6435 (2016). doi:10.1080/14786435.2016.1200758.
[44] V. Sabelová, V. Kršjak, J. Kuriplach, M. Petriska, V. Slugeň, J. Šimeg Veterníková, Characterization of helium implanted Fe-Cr alloys by means of positron annihilation methods, J. Nucl. Mater. 450 (2014) 54–58, https://doi.org/10.1016/j.jnucmat.2013.10.039.
[45] R. Kögler, W. Anwand, A. Richter, M. Butterling, A. Mücklich, Investigation of dual-beam-implanted oxide-dispersed-strengthened FeCrAl alloy by positron annihilation spectroscopy, 331 (2012) 149–163. doi:10.4028/www.scientific.net/DDF.331.149.
[46] E. Lu, X. Cao, S. Jin, P. Zhang, C. Zhang, J. Yang, Y. Wu, L. Guo, B. Wang, Investigation of vacancy-type defects in helium irradiated FeCrNi alloy by slow positron beam, J. Nucl. Mater. 458 (2015) 240–244, https://doi.org/10.1016/J.JNUCMAT.2014.12.070.